Cyclically Operated Microwave Single-Photon Counter with Sensitivity of 10^{-22} W/$\sqrt{\text{Hz}}$

L. Balembois,[1] J. Travesedo,[1] L. Pallegoix,[1] A. May,[1,2] E. Billaud,[1] M. Villiers,[3] D. Estève,[1] D. Vion,[1] P. Bertet,[1] and E. Flurin[1,*]

[1] *Université Paris-Saclay, CEA, CNRS, SPEC, 91191 Gif-sur-Yvette Cedex, France*
[2] *Alice&Bob, 53 boulevard du Général Martial Valin, 75015 Paris*
[3] *Laboratoire de Physique de l'Ecole Normale Suprérieure, Paris, France*

(Received 7 July 2023; revised 14 December 2023; accepted 21 December 2023; published 23 January 2024)

Single-photon detection played an important role in the development of quantum optics. Its implementation in the microwave domain is challenging because the photon energy is five orders of magnitude smaller. In recent years, significant progress has been made in developing single microwave photon detectors (SMPDs) based on superconducting quantum bits or bolometers. In this paper we present a practical SMPD based on the irreversible transfer of an incoming photon to the excited state of a transmon qubit by a four-wave mixing process. This device achieves a detection efficiency $\eta = 0.43$ and an operational dark count rate $\alpha = 85$ s^{-1}, mainly due to the out-of-equilibrium microwave photons in the input line. The corresponding power sensitivity is $\mathcal{S} = 10^{-22}$ W/$\sqrt{\text{Hz}}$, one order of magnitude lower than the state of the art. The detector operates continuously over hour time-scales with a duty cycle $\eta_D = 0.84$, and offers frequency tunability of at least 50 MHz around 7 GHz.

DOI: 10.1103/PhysRevApplied.21.014043

I. INTRODUCTION

Single-photon detection is a mature technique in the optical domain. Its applications are numerous, ranging from fluorescence microscopy [1–4] to measurement-based quantum computing [5]. At microwave frequencies (5–10 GHz), single-photon detection is more challenging due to the five orders of magnitude photon energy, requiring in particular millikelvin temperatures to minimize the number of thermal photons per mode. Nevertheless, a range of applications make the development of such devices relevant. Single microwave photon detectors (SMPDs) have been proposed for detecting weak incoherent emitters at microwave frequencies, such as electron spins in solids [6–8] or hypothetical dark matter candidate particles [9,10]. SMPDs may also be useful for primary thermometry [11] and for quantum illumination protocols [12]. Finally, SMPDs will enable the implementation of several quantum information processing protocols [13–15], for instance for the heralded entanglement of superconducting qubits at a distance [16], the development of new qubit readout schemes [17], and the robust generation of quantum states [18].

SMPD designs based either on superconducting quantum bits or bolometers have been proposed [19–27] and implemented [16,28–33]. Besides itinerant microwave photon detectors, other experiments have demonstrated high-sensitivity detection of individual microwave photons in a high-Q cavity [10,34,35].

The detection sensitivity, as well as the fidelity of the envisioned quantum protocols, depend crucially on the SMPD characteristics. Two figures of merit especially matter: the dark count rate α, defined as the number of false-positive detections per unit of time, and the operational efficiency η, defined as the ratio of counts to incoming photons. Combining these two metrics, one can determine the power sensitivity $\mathcal{S}$ of the detector as the noise- equivalent power (NEP) for an integration time of 1 s (see Appendix C):

$$\mathcal{S} = \frac{\hbar\omega\sqrt{\alpha}}{\eta}. \tag{1}$$

Currently, detectors based on superconducting qubits [30–32] show a dark count rate $\alpha \sim 10^4$–10^5 s^{-1}, for an efficiency $\eta \sim 0.5$–0.7 over a bandwidth of about 10–20 MHz, resulting in a sensitivity $\mathcal{S} \sim 2$–9×10^{-21} W/$\sqrt{\text{Hz}}$ at 7 GHz. On the other hand, the most advanced bolometric detector based on graphene [33] reaches a sensitivity $\mathcal{S} = 7 \times 10^{-19}$ W/$\sqrt{\text{Hz}}$ at 7.9 GHz, when operated at 190 mK. The bandwidth of this device varies between 861 MHz and 599 MHz depending on the operating parameters.

This article presents an SMPD based on a superconducting qubit and a four-wave mixing process [36]. It detects

*emmanuel.flurin@cea.fr

itinerant photons, regardless of their waveform, in a bandwidth of about 1 MHz around a frequency tunable from 7.005 GHz to at least 6.955 GHz (see Appendix B) and operates in cycles of approximately 12 μs duration, which can be repeated continuously over several hours, days, or even months. Here we demonstrate, at the specific frequency of 6.979 GHz, a dark count rate $\alpha = 85\ \mathrm{s}^{-1}$ for an operational efficiency $\eta = 0.43$ leading to a power sensitivity $\mathcal{S} = 10^{-22}\ \mathrm{W}/\sqrt{\mathrm{Hz}}$, more than an order of magnitude lower than the state of the art. This new sensitivity has opened up new detection possibilities. In particular, a device (called SMPD2 in Appendix I) very similar to the one discussed in this work has recently enabled the detection of individual electron spins in solids, through their microwave fluorescence [8].

II. WORKING PRINCIPLE

This device builds upon the superconducting circuit proposed and demonstrated in Refs. [6,36]. The working principle is based on the irreversible transfer of an incoming photon to an excitation of a transmon qubit. The detector "clicks" when the qubit is detected in its excited state using a dispersive readout through a capacitively coupled resonator.

This irreversible transfer is achieved by a four-wave mixing process, directly provided by the transmon qubit Hamiltonian. The incoming photon impinging on an input resonator with frequency ω_b [called "buffer" mode, orange in Fig. 1(a)] combines with a pump tone at frequency ω_p and is converted into an excitation in the transmon qubit mode at frequency ω_q and an additional photon in an output resonator mode at frequency ω_w [called "waste" mode, green in Fig. 1(a)]. This four-wave mixing process is described by the Hamiltonian

$$\hat{H}_{4\mathrm{wm}} = \sqrt{\chi_b \chi_w}\left(\xi \hat{b}\hat{\sigma}^{\dagger}\hat{w}^{\dagger} + \xi^{*}\hat{b}^{\dagger}\hat{\sigma}\hat{w}\right), \qquad (2)$$

where $\hat{b}$ and $\hat{w}$ are respectively the annihilation operators corresponding to the buffer mode and waste mode, $\hat{\sigma}$ is the lowering operator corresponding to the qubit, ξ is the pump amplitude in the qubit mode, and χ_b and χ_w are respectively the dispersive shifts of the transmon qubit with respect to the buffer and waste modes [36]. For this process to be activated, the pump frequency is tuned such that $\omega_p + \omega_b = \omega_q + \omega_w - \chi_w$, to satisfy the four-wave mixing resonance condition.

The irreversibility of the conversion is ensured by the coupling of the waste resonator to a dissipative environment. While the qubit remains excited, the photon in the waste resonator leaks out in the measurement line at the rate κ_w. The reciprocal four-wave mixing process [second term in parentheses in Eq. (2)] is therefore suppressed and the qubit is left in its excited state. The detector behaves as an energy integrator, which is independent of the incoming photon waveform provided that its spectral extension

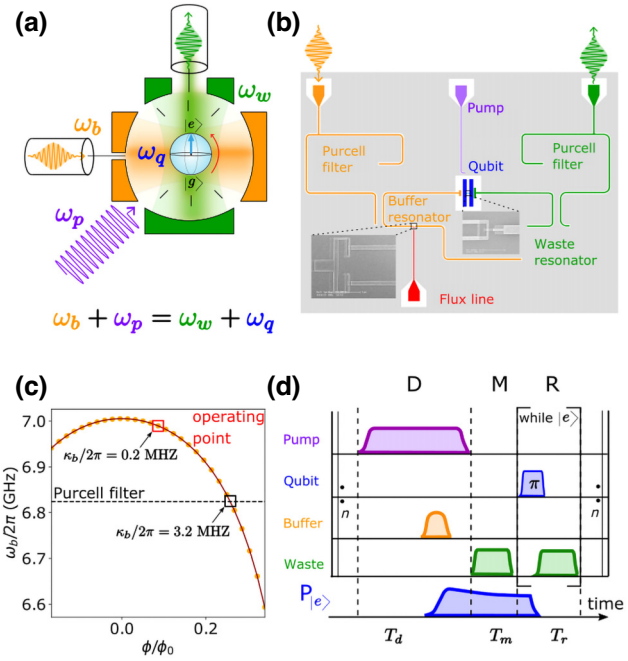

FIG. 1. (a) Principle of the photon detector. Two cavities, buffer (orange) and waste (green), are coupled to a transmon qubit whose nonlinearity allows the modes to be mixed. A pump tone (purple) triggers a four-wave mixing process, converting an incoming buffer photon into a long-lived qubit excitation and a waste photon quickly dissipated into the environment, making the reversal process impossible. (b) Schematic of the SMPD chip. The transmon qubit (blue) at frequency $\omega_q/2\pi = 6.184$ GHz is capacitively coupled to two coplanar waveguide resonators: the buffer [see (c)] and the waste ($\omega_w/2\pi = 7.704$ GHz, $\kappa_w/2\pi = 1.8$ MHz). Two Purcell filters are added to protect the qubit from radiative relaxation. The tunability of the detector is ensured by inserting a superconducting quantum interference device (SQUID), driven by a flux line (red), in the buffer resonator. (c) Evolution of the buffer frequency with the respect to the magnetic flux through the SQUID. Orange points are data, the solid red line is a fit, and the dashed black line represents the buffer Purcell filter frequency. Due to the frequency detuning between the buffer and its filter, the buffer bandwidth κ_b varies with its frequency. The red square represents the operating point. (d) Cyclic operation of the SMPD consisting of three steps repeated continuously. The detection window (D) involves switching on the pump tone (purple) for $T_d = 10$ μs to allow the conversion of the incoming photon (orange). The measurement window (M) involves applying a readout pulse (green) on the waste resonator to measure the qubit state. The reset window (R) is a conditional loop to reinitialize the qubit in its ground state. The excited population of the qubit during the pulse sequence is represented below. The average detector blind time is $T_m + T_r = 1.9$ μs.

remains included than the frequency linewidth of the buffer mode.

The four-wave mixing being a resonant process, it is intrinsically narrowband. To make it a practical detector, our device is made frequency tunable to match the photon frequency of interest by inserting a superconducting quantum interference device (SQUID) in the buffer resonator [see Fig. 1(b)]. The detector frequency can be tuned from $\omega_b/2\pi = 7.005$ GHz over several hundred megahertz [see Fig. 1(c)]. Two bandpass Purcell filters are associated with the resonators to prevent spurious decay of the qubit into the lines [37]. Therefore, the buffer resonator linewidth depends on its frequency detuning with respect to its Purcell filter. The bandwidth $\kappa_b/2\pi = 3$ MHz is maximal for $\omega_b/2\pi = 6.824$ GHz. In the following, the detector is characterized at $\omega_b/2\pi = 6.979$ GHz and $\kappa_b/2\pi = 0.2$ MHz. The resonance frequencies of the waste resonator $\omega_w/2\pi = 7.704$ GHz and the transmon qubit $\omega_q/2\pi = 6.184$ GHz are fixed. The relaxation time T_1 of the transmon qubit is measured as $T_1 \sim 37$ µs [see Fig. 2(d)] and its equilibrium population fluctuates around $p_{\text{eq}} \sim 2\text{–}4 \times 10^{-4}$ [see Figs. 2(c) and 2(d)], close to the lowest reported [38–41]. For the particular value $\omega_b/2\pi = 6.935$ GHz, the pump tone set by the four-wave mixing resonance condition becomes resonant with the buffer resonator. Under such conditions, the pump couples directly to the buffer, the four-wave mixing becomes degenerate, and the SMPD cannot operate. This collision between the pump and buffer frequencies is due to fabrication inaccuracies and has been corrected in the second version of the design (SMPD2; see Appendix I).

The optimal pump characteristics (frequency $\omega_p/2\pi$ and amplitude ξ) are determined experimentally by monitoring the qubit population while illuminating the buffer mode with a weak coherent signal and by sweeping the pump tone frequency and amplitude. As shown in Fig. 2(b), a large excited state population is found in the qubit state conditioned on the presence of the illuminating tone for a pump frequency of $\omega_p/2\pi = 6.885$ GHz. This value is in good agreement with the mode frequencies, taking into account the qubit Stark shift induced by the pump and the dispersive shift of the resonators.

In a restricted subspace where buffer and waste are never simultaneously populated, our device can be described by two cavities coupled with the strength $g_3 = 2|\xi|\sqrt{\chi_b\chi_w}$ [6] (see Appendix D). In this framework, the maximum detection efficiency is expected when the coupling strength g_3 matches the geometric mean of decay rates of the buffer and waste resonators such that $2|\xi|\sqrt{\chi_b\chi_w} = \sqrt{\kappa_b\kappa_w}$ [36]. The model also provides an explicit formula for the transfer efficiency $\eta_{4\text{wm}}$ between a buffer photon and a qubit excitation:

$$\eta_{4\text{wm}} = \frac{4C}{(1+C)^2}, \tag{3}$$

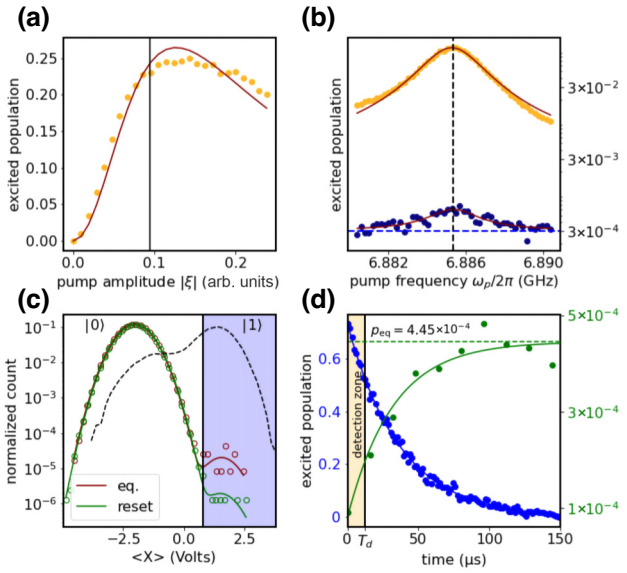

FIG. 2. (a) Qubit-excited population as a function of the pump amplitude $|\xi|$ applied to the qubit when a coherent tone of 360 zW (77 850 photons per second) is applied on the buffer resonator. The pump frequency is adapted for each amplitude to follow the Stark shift. Orange points are data, the dark red solid line represents a fit using (3), and the black solid line represents the chosen amplitude. (b) Qubit-excited population as a function of the pump frequency $\omega_p/2\pi$ when no signal is sent to the buffer (dark blue) and when a coherent tone (360 zW) is applied (orange). Solid red lines represent Lorentzian fit, and the dashed black line is the center of the resonance. (c) Qubit readout when no pulses are applied to the qubit (red), giving a qubit equilibrium population $p_{\text{eq}} = 2 \times 10^{-4}$, and qubit readout just after a reset sequence (green), giving a reset population $p_{\text{reset}} = 10^{-5}$. Solid lines represent Gaussian fit. The dashed black line represents the qubit readout after a π-pulse, and the vertical solid line corresponds to the chosen readout threshold. (d) Qubit relaxation curve from the excited state (blue) and from the ground state (green). Solid lines represent exponential fits. The yellow window corresponds to the detection time $T_d = 10$ µs.

where $C = 4|\xi|^2\chi_b\chi_w/\kappa_b\kappa_w$ is the cooperativity associated with the four-wave mixing. Unit transfer efficiency is reached for $C = 1$. Taking into account resonator losses, we expect a maximum transfer efficiency of $\eta_{4\text{wm}} = 0.86$ (see Appendix E). To determine the pump amplitude corresponding to the optimal cooperativity, we operate the four-wave mixing for various pump amplitudes by sending photons to the buffer resonator. The resulting qubit-excited population, plotted in Fig. 2(a), is in good agreement with the theoretical two-coupled-cavities model. We have chosen to operate slightly below the optimum pump amplitude to mitigate the heating effects.

In order to avoid spurious qubit heating due to the pump tone, a low pump amplitude is desirable. This is conveniently achieved if the dispersive shifts $\chi_{b,w}$ are larger than the $\kappa_{b,w}$. Here, the measured dispersive shifts

are $\chi_b/2\pi = 5.2$ MHz, $\chi_w/2\pi = 18.8$ MHz and the resonators linewidths $\kappa_b/2\pi = 0.2$ MHz (at the point considered) and $\kappa_w/2\pi = 1.8$ MHz. At unit cooperativity, the pump energy is $|\xi|^2 = 5 \times 10^{-3}$ in units of qubit excitation. Note that the large dispersive shift between the resonators and the qubit is not detrimental for two reasons. First, the maximum number of excitation in modes during the transfer process never exceeds one, so that higher-order nonlinear terms do not contribute significantly to the dynamics as shown on Fig. 2(b). Second, Purcell filters at the output of each of the resonators inhibit the spurious decay of the qubit into transmission lines.

III. CYCLIC OPERATION

The detector is operated cyclically, with the operation cycle consisting of three subsequent steps [see Fig. 1(d)]. The first, "detection" (D), involves applying to the qubit a pump pulse at frequency ω_p for a detection time $T_d = 10$ μs (see Appendix G for T_d calibration). If a photon enters into the buffer resonator, the four-wave mixing process triggers a qubit excitation and the dissipation of a photon into the waste resonator.

In the second step of the cycle, "measurement" (M), the qubit state is dispersively read out using the waste resonator for a measurement time $T_m = 0.5$ μs. Note that the threshold used to discriminate the qubit ground and excited states is chosen to maximize the SMPD power sensitivity defined in Eq. (1). As shown in Fig. 2(c), this threshold favors the readout fidelity of the ground state at the expense of the readout fidelity of the excited state $p(1|e) = \eta_{\mathrm{RO}} = 0.73$. The dark count is minimized at the expense of a moderate reduction in efficiency.

The third step of the cycle consists of a conditional reset (R). If the qubit is previously found in its ground state, we directly go to the next cycle. If the qubit was found in its excited state, a π-pulse is applied though the pump line and the qubit state is measured again, the procedure being repeated until the ground preparation succeeds. Owing to the high fidelity of the qubit ground-state readout, we reset the qubit well below its equilibrium population p_{eq} as shown in Fig. 2(d); the reset infidelity is as low as $p_{\mathrm{reset}} = 10^{-5}$. The reset step is nondeterministic, with an average reset time $T_r \approx 0.5$ μs. For the reset to work optimally, the quantum nondemolition character of the measurement must be ensured. To meet this condition, we use a traveling wave parametric amplifier and we carefully tune the readout pulse length and amplitude. Moreover, the readout pulse frequency is detuned with the respect to the waste resonator frequency by the dispersive shift of the qubit, such that the readout pulse enters the resonator if and only if the qubit is in its excited state. This allows us to enhance the quantum nondemolition character of the measurement when the qubit is in its ground state.

A waiting time of 1 μs is added at the end of the reset step to let the waste resonator return to its ground state. The average cycle time is $T_{\mathrm{cycle}} = 11.9$ μs, which sets the duty cycle of the detector $\eta_D = T_d/T_{\mathrm{cycle}} = 0.84$. This quantity could be made arbitrarily close to 1 by increasing the duration of the detection window. However, the qubit relaxation in a characteristic time $T_1 = 37$ μs [see Fig. 2(d)] sets an upper bound, by introducing a contribution $\eta_{\mathrm{qubit}} = (T_1/T_d)(1 - e^{-T_d/T_1})$ to the overall efficiency, which actually limits the detection step duration.

The detector is operated by continuously repeating the cycle about 8×10^4 times per second. Its temporal resolution is determined by the detection time $T_d = 10$ μs, whereas its dead time is $T_m + T_{\mathrm{reset}} = 1.9$ μs.

IV. DETECTION EFFICIENCY

The operational efficiency is measured by sending a calibrated tone at the center of the SMPD line [see Fig. 3(d)] while the cycle is repeated. The power of the microwave tone is calibrated by using the dephasing of the qubit induced by the presence of photons in the buffer cavity [42].

Typical measurement records of the detector for various illumination powers are shown Fig. 3(a). The operational efficiency of the SMPD, $\eta = 0.43$, is obtained by measuring the ratio between the click event rate and the incoming photon rate as shown in Fig. 3(b). The efficiency is in good agreement with the expected one that includes four different contributions: the transfer efficiency $\eta_{4\mathrm{wm}}$, the qubit relaxation η_{qubit}, the duty cycle η_D and the readout fidelity η_{RO} resulting in a theoretical efficiency $\eta_{\mathrm{theory}} = \eta_{4\mathrm{wm}} \cdot \eta_{\mathrm{RO}} \cdot \eta_D \cdot \eta_{\mathrm{qubit}} = 0.46$.

V. DETECTION BANDWIDTH

The detector bandwidth is measured by varying the frequency of a 10-μs photon pulse sent to the buffer resonator during the detection window. The qubit excitation probability is measured and multiplied by a constant factor so that the maximum value corresponds to the overall efficiency $\eta = 0.43$. This inferred efficiency is then plotted with the respect to the frequency of the input photons as shown in Fig. 3(d). The detector bandwidth, defined as the full width at half maximum (FWHM), is $\kappa_d/2\pi = 0.57$ MHz.

From a model of two coupled cavities (see Appendix D), explicitly derived in Ref. [6], we can obtain an analytical expression for κ_d with respect to κ_b and κ_w:

$$\kappa_d = \sqrt{2}\sqrt{\sqrt{\kappa_b^2\kappa_w^2 + \left(\frac{\kappa_b - \kappa_w}{2}\right)^4} - \left(\frac{\kappa_b - \kappa_w}{2}\right)^2}, \quad (4)$$

yielding the theoretical $\kappa_{d,\mathrm{th}}/2\pi = 0.43$ MHz. Here $\kappa_{d,\mathrm{th}} \approx 2\kappa_b$ which corresponds to the limit where $\kappa_w \gg \kappa_b$. We

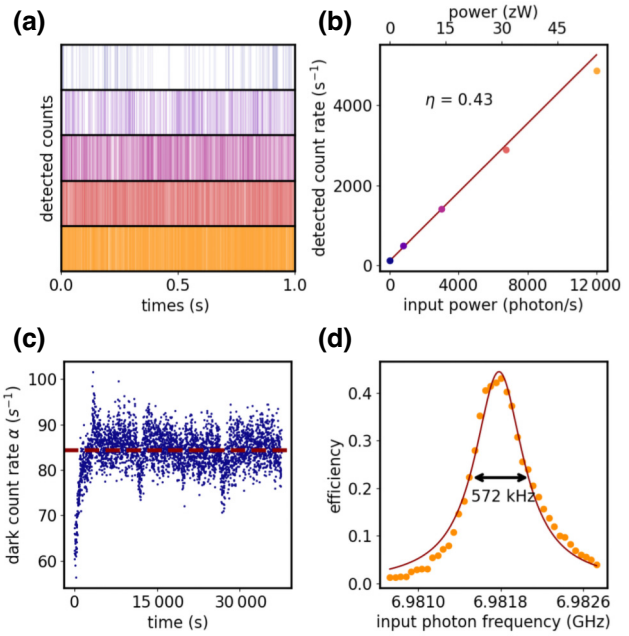

FIG. 3. (a) Time traces of the SMPD operated in cyclic mode; each vertical line represents one photon detection. The power of the coherent tone sent to the buffer resonator is progressively increased from 0 W (dark blue) to 54 zW (12 000 photons per second) (orange). (b) Detected count rate as a function of incoming photon rate. The efficiency η is extracted with a linear fit (solid line). The deviation from the linear behavior is due to the detector saturation. (c) Dark count rate as the function of time. Each point is the average rate over approximately 12 s, which corresponds to 10^6 cycles. The dashed line represents the dark count saturation $\alpha = 85\ \mathrm{s}^{-1}$. (d) Inferred efficiency of the SMPD as a function of the frequency of the coherent tone applied to the buffer resonator. The power of the tone is still 360 zW. Solid lines represent a Lorentzian fit. The detector bandwidth defined as the full width at half maximum is $\kappa_d/2\pi = 0.57$ MHz.

attribute the discrepancy between the theoretical and the measured bandwidth to the 100 kHz spectral broadening caused by the finite length of the excitation pulses.

VI. DARK COUNTS

The dark count rate is estimated by measuring the count rate of the detector in the absence of input photons as illustrated in the top panel of Fig. 3(a). The dark count rate is found to be 60 s^{-1} for a few minutes' operation. As shown in Fig. 3(c), when operated on an hour time-scale, we observe a slight rise of the dark count rate to 85 s^{-1} over a period of 1 h, after which it remains stable within $\pm 4\ \mathrm{s}^{-1}$ over 10 h. The initial dark count rise is attributed to the heating of the cold stage of the refrigerator due to the continuous power delivered by the qubit pump. The sensitivity of the detector in steady state regime is then simply given by Eq. (1) and yields a value $\mathcal{S} = 10^{-22}\ \mathrm{W}/\sqrt{\mathrm{Hz}}$.

VII. DARK COUNT BUDGET

The dark counts α can be decomposed into three main contributions: the thermal population of the qubit α_{qubit}, the heating of qubit by the pump $\alpha_{4\mathrm{wm}}$, and the presence of thermal photons in the input lines α_{th}. The resulting dark count rate is the sum of the three contributions: $\alpha = \alpha_{\mathrm{qubit}} + \alpha_{4\mathrm{wm}} + \alpha_{\mathrm{th}}$, each of which can be addressed individually.

The first contribution is the probability of finding the qubit in its excited state in the absence of the four-wave mixing process. This depends on the qubit excitation probability after the reset p_{reset} and the relaxation rate T_1^{-1} of the qubit toward its equilibrium population p_{eq} [see Figs. 2(c) and 2(d)] such that $\alpha_{\mathrm{qubit}} = (p_{\mathrm{eq}}/T_1)\eta_D + p_{\mathrm{reset}}/T_{\mathrm{cycle}}$. We evaluate this contribution to $\alpha_{\mathrm{qubit}} = 5\ \mathrm{s}^{-1}$ by using the parameters $p_{\mathrm{eq}}, T_1, p_{\mathrm{reset}}, \eta_D$ and T_{cycle} defined in the previous sections. To mitigate this source of noise, the qubit is thermalized by filtering the line on a broad frequency range up to the infrared domain (eccosorb filter) and by properly designing an electromagnetic shield composed of three interleaved screens in μ-metal, copper and aluminum.

The second contribution is the spurious heating of the qubit by the pump tone $\alpha_{4\mathrm{wm}}$. This contribution is measured by applying a pump tone detuned from the four-wave mixing condition while measuring the equilibrium population of the qubit. As shown in Fig. 2(b), in these conditions $p_{\mathrm{eq}} = 3 \times 10^{-4}$, a value included in the fluctuation interval of the equilibrium population. This contribution to the overall dark count rate is therefore considered negligible.

The third contribution, α_{th}, is due to the presence of spurious photons in the input transmission lines. The integration of the mean number of photons per mode in the buffer input line $\bar{n}_b$ over the linewidth of the detector κ_d gives the corresponding dark count rate $\alpha_{\mathrm{th}} = 80\ \mathrm{s}^{-1}$. At the cryostat base temperature (10 mK), this contribution should be negligible as the Planck law would predict an average number of photons per mode $\bar{n}_b = 3 \times 10^{-15}$; however, it is notoriously difficult to thermalize the microwave field at such low temperatures. Based on a Johnson-Nyquist description of thermal noise, we can derive the explicit relation [43] (see Appendix F)

$$\alpha_{\mathrm{th}} = \frac{\kappa_d}{4}\eta\bar{n}_b. \tag{5}$$

To verify the validity of this relation, we measure the thermal dark count as the function of a well-defined mode population, that is, when the refrigerator temperature is above 40 mK. This temperature is measured by a thermometer anchored to the mixing chamber plate. We acquired the dark count rate α in a range from 10 mK to 100 mK, waiting for the end of the transient regime each time. Since the heating is not selective, all parts of the chip are affected, including the transmon qubit which causes an increase in its equilibrium population p_{eq} and a decrease in

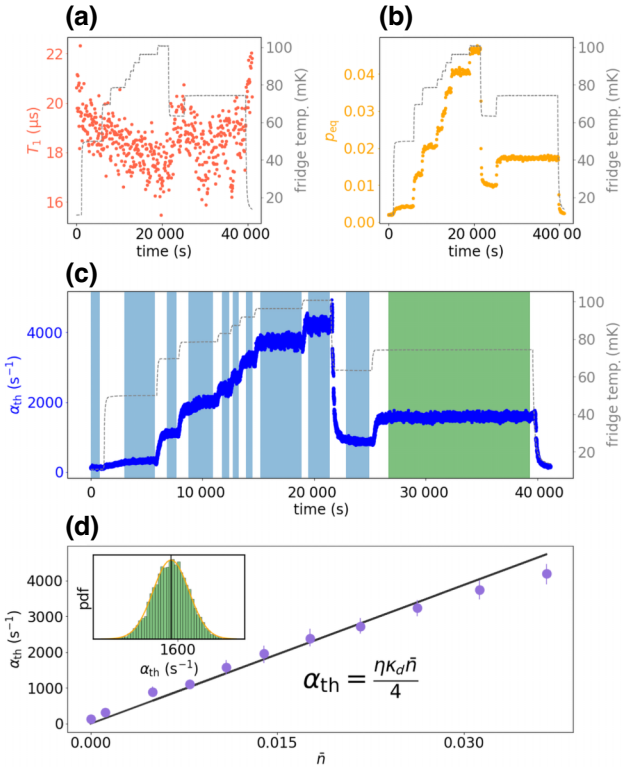

FIG. 4. Johnson-Nyquist law demonstrated with the SMPD. Qubit relaxation time T_1 (a) and qubit equilibrium population p_{eq} (b) taken every minute. These values are used to determine the value of α_{qubit}. The fridge temperature is shown in dashed gray lines. (c) Thermal dark count rate $\alpha_{th} = \alpha - \alpha_{qubit}$ for different refrigerator temperatures shown in dashed gray lines. Each point corresponds to the average dark count rate over 10^5 cycles; the light blue areas correspond to the data selected to extract the averages by avoiding the transient regime. (d) Relation between the mode population $\bar{n}_b$, calculated from the refrigerator temperature, and the thermal dark count rate α_{th}. Each point (purple) corresponds to the average of the colored areas of (c); an example of distribution is given in the inset for the green zone. The solid line correspond to the Johnson-Nyquist relation where η is the SMPD efficiency and κ_d the SMPD bandwidth.

its relaxation time T_1. To take these effects into account, these two quantities are measured every minute during the experiment [Figs. 4(a) and 4(b)], giving minute-by-minute monitoring of α_{qubit}. Note that the relaxation time is now of the order of 20 μs, compared with 37 μs in the previous sections. This decrease appeared for an unknown reason after a few cooldown cycles.

The thermal dark count rate $\alpha_{th} = \alpha - \alpha_{qubit}$ is plotted as a function of time [see Fig. 4(c)] and with the respect to the thermal photon population $\bar{n}_b$ calculated from the refrigerator temperature [see Fig. 4(d)]. The relationship between α_{th} and $\bar{n}_b$ is linear with a slope of $\eta\kappa_d/4$, therefore validating Eq. (5).

As explained earlier, at 10 mK, $\bar{n}_b$ is decoupled from the refrigerator temperature, but we can estimate an equivalent electromagnetic temperature from the dark count measurement. At 10 mK, the measured dark count is $\alpha = 85\ s^{-1}$ [see Fig. 3(c)], as we evaluate α_{qubit} to $5\ s^{-1}$' the equivalent α_{th} is $80\ s^{-1}$, corresponding to $\bar{n}_b = 6.5 \times 10^{-5}$. By using Eq. (5), the equivalent electromagnetic temperature of the input line is 35 mK.

In principle, one could further improve the SMPD performance by improving the attenuation of the lines. However, the temperature of the microwave radiations is challenging to reduce arbitrarily close to the cryostat base temperature as it requires a large amount of attenuators that are thermally well anchored.

VIII. CONCLUSION

We have demonstrated the operation of a single microwave photon detector based on a four-wave mixing process.

The efficiency of the device reaches 0.43 and is quantitatively understood from the contributions of the detector duty cycle, the qubit ability to store an excitation, the qubit readout, and the four-wave mixing efficiency. It can be improved in future devices with longer transmon relaxation times (see Appendix H), noting that qubit T_1s up to several hundred microseconds have been demonstrated [44,45].

The second key quantity studied in this article is the dark count rate. We have demonstrated that most of these false-positive events are caused by spurious photons due to the electromagnetic temperature of the line. A direct way of lowering the dark count would be to reduce the detector bandwidth so that it matches the bandwidth of the measured system.

Utilizing these metrics, the power sensitivity of the SMPD is determined as $\mathcal{S} = \hbar\omega(\sqrt{\alpha}/\eta) = 10^{-22}\ \mathrm{W}/\sqrt{\mathrm{Hz}}$. We have also verified the direct relation between the count rates and the thermal occupation of the lines, opening the way to using the SMPD as an absolute thermometer in the 10–100 mK range.

Even though further improvements of the device performance are desirable in the future, its high sensitivity has already enabled new experiments, such as single-spin electron spin resonance spectroscopy [8], as well as proof-of-principle axion search.

ACKNOWLEDGMENT

We acknowledge technical support from P. Sénat, D. Duet, P.-F. Orfila and S. Delprat, and are grateful for fruitful discussions within the Quantronics group. We acknowledge support from the Agence Nationale de la Recherche (ANR) through the DARKWADOR (ANR-19-CE47-0004) projects. We acknowledge support of the Région Ile-de-France through the DIM SIRTEQ (REIMIC project), from the AIDAS virtual joint laboratory, and from the France 2030 plan under the ANR-22-PETQ-0003

grant. This project has received funding from the European Research Council under Grant No. 101042315 (INGENIOUS). We acknowledge IARPA and Lincoln Labs for providing the Josephson traveling-wave parametric amplifier.

APPENDIX A: EXPERIMENTAL PARAMETERS OF THE DEVICE

Table I summarizes the various parameters of the device. The parameter ω_{Pw} (ω_{Pb}) is the frequency of the waste (buffer) Purcell filter. κ_{Pb}, κ_{Pw} are the filters bandwidth. $E_c/2$ is the anharmonicity of the qubit. $\kappa_{b,\mathrm{ext}}(\kappa_{b,\mathrm{int}})$ is the coupling (internal) losses of the buffer resonator and $\kappa_{w,\mathrm{ext}}(\kappa_{w,\mathrm{int}})$ is the coupling (internal) losses of the waste resonator.

APPENDIX B: OTHER OPERATING POINTS

In the main text, we present the SMPD for the specific buffer frequency $\omega_b/2\pi = 6.979$ GHz. In this section, we present the dark count and the efficiency of the detector at two other buffer frequencies: $\omega_b/2\pi = 6.9697$ GHz and $\omega_b/2\pi = 6.9549$ GHz.

The efficiency is measured by sending a coherent wave packet of amplitude b_{in} to the buffer for a time t_b, while the four-wave mixing is activated by the pump tone [see Fig. 5(a)]. The photon flux corresponding to the amplitude b_{in} is calibrated using a Ramsey experiment perturbed by a field sent to the buffer (see [43] for more details). For each time t_b we measure the ratio between the number of photons sent and the qubit-excited population, which gives the detector efficiency without the duty cycle contribution: η/η_D. As shown in Fig. 5(c), due to the buffer bandwidth, the efficiency grows with t_b until it reaches an asymptote corresponding to η/η_D. Taking into account the duty cycle $\eta_D = 0.84$, we get $\eta = 0.41$ for $\omega_b/2\pi = 6.9697$ GHz and $\eta = 0.34$ for $\omega_b/2\pi = 6.9549$ GHz.

The dark count rate α is measured by repeating the detection cycle Nn times, where N is the number of experiments, and $n = 12500$ is the number of detection cycles of $t_{\mathrm{cycle}} = 11.8$ μs per experiment. For each experiment, the number of clicks per second is averaged over $k = 500$ cycles and plotted as a function of time in Fig. 5(d). We get $\alpha = 125\ \mathrm{s}^{-1}$ for $\omega_b/2\pi = 6.9697$ GHz and $\eta = 90\ \mathrm{s}^{-1}$ for $\omega_b/2\pi = 6.9549$ GHz.

These figures give a sensitivity of $\mathcal{S} \approx 1.2 \times 10^{-22}\ \mathrm{W}/\sqrt{\mathrm{Hz}}$ for both buffer frequencies, comparable to the sensitivity shown in the main text.

TABLE I. Parameters of the SMPD1 components. The buffer frequency is shown for 3 significant values of the flux in the SQUID loop corresponding to: the maximum frequency, the operating frequency in the main text and the resonance frequency with respect to the Purcell filter.

Qubit			
$\omega_q/2\pi$			6.184 GHz
$E_c/4\pi$			∼ 240 MHz
$\chi_b/2\pi$			5.2 MHz
$\chi_w/2\pi$			18.8 MHz
T_1			∼37 μs
T_2			∼56 μs
p_{eq}			$\sim 2 \times 10^{-4}$
Buffer	$\phi/\phi_0 = 0$	$\phi/\phi_0 = 0.11$	$\phi/\phi_0 = 0.25$
$\omega_b/2\pi$	7.005 GHz	6.979 GHz	6.824 GHz
$\kappa_{b,\mathrm{ext}}/2\pi$	0.152 MHz	0.172 MHz	2.95 MHz
$\kappa_{b,\mathrm{int}}/2\pi$	0.100 MHz	0.028 MHz	nc
Waste			
$\omega_w/2\pi$			7.704 GHz
$\kappa_{w,\mathrm{ext}}/2\pi$			1.72 MHz
$\kappa_{w,\mathrm{int}}/2\pi$			0.11 MHz
Filters			
$\omega_{Pb}/2\pi$			6.824 GHz
$\kappa_{Pb}/2\pi$			84.2 MHz
$\omega_{Pw}/2\pi$			7.620 GHz
$\kappa_{Pw}/2\pi$			180 MHz

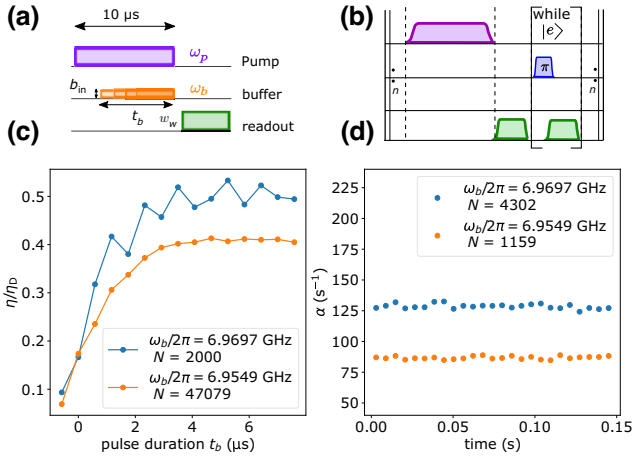

FIG. 5. (a) Pulse sequence used to measure efficiency. A pump tone (purple pulse) of duration 10 μs is sent to the qubit mode, and an incoming coherent wave packet (orange pulse) of duration t_b and amplitude b_{in} is applied to the buffer. The qubit-excited state population p_e is detected by the waste (green pulse). (b) Cycle similar to the main text repeated $n = 12\,500$ times per experiment. (c) Efficiency η/η_D as a function of wave-packet duration t_b, measured with sequence (a). Each point is averaged N times. (d) Dark count measured over $n = 12\,500$ cycles of $t_{\mathrm{cycle}} = 11.8$ μs. Each point corresponds to the average of $k = 500$ cycles. The experiment is repeated N times and averaged.

APPENDIX C: NOISE-EQUIVALENT POWER

The NEP is defined as the minimum detectable power with a signal-to-noise ratio (SNR) of 1 for a certain integration time t. This quantity, expressed in $\mathrm{W}/\sqrt{\mathrm{Hz}}$, provides

a good representation of the absolute sensitivity of the SMPD.

We will first write the SNR considering that the detected signal is provided by a continuous tone of power P, at resonance with the buffer resonator and with a Poisson noise. When this microwave tone is turning ON, the number of photons impinging the detector for a time t is $Pt/\hbar\omega_b$. Due to the dark count rate and the efficiency, the number of clicks given by the detector is $S_{\mathrm{ON}} = \eta Pt/\hbar\omega_b + \alpha t$. In contrast, when the microwave tone is OFF, the signal integrated by the detector for a time t is $S_{\mathrm{OFF}} = \alpha t$.

The signal of interest is $S_{\mathrm{int}} = S_{\mathrm{ON}} - S_{\mathrm{OFF}} = \eta Pt/\hbar\omega_b$. As all the distributions are Poisson, the associated noise is $N_{\mathrm{int}} = \sqrt{S_{\mathrm{ON}} + S_{\mathrm{OFF}}}$. Assuming that the dark count is perfectly known, we can reduce the expression of the noise to $N_{\mathrm{int}} = \sqrt{S_{\mathrm{ON}}}$.

The SNR of the detection is then given by

$$\mathrm{SNR} = \frac{\eta Pt/\hbar\omega_b}{\sqrt{Pt/\hbar\omega_b + \alpha t}}. \tag{C1}$$

The NEP is given by the power P corresponding to SNR $=$ 1, yielding

$$\mathrm{NEP} = \frac{\hbar\omega_b(1 + \sqrt{1 + 4t\alpha})}{2t\eta}. \tag{C2}$$

In this paper, the integration time is set such that $\sqrt{\alpha t} \gg 1$ reducing the NEP to

$$\mathrm{NEP} = \hbar\omega_b \frac{\sqrt{\alpha}}{\eta\sqrt{t}}. \tag{C3}$$

APPENDIX D: TWO-COUPLED-CAVITIES MODEL

The detector response can be modeled by considering that the buffer and waste resonator are coupled with a constant $\mathcal{G} = -\xi_p\sqrt{\chi_{qb}\chi_{qw}}$ due to the four-wave parametric process involving the qubit, where ξ_p is the pump amplitude in units of square root of photons and χ_{qb} (χ_{qw}) the dispersive coupling of the buffer (waste) resonator to the qubit. We can write down the system of coupled equations for the buffer and waste intraresonator fields ν and β, assuming that the resonators are lossless:

$$\dot{\nu} = -i\delta_b\nu - i\mathcal{G}\beta - \frac{\kappa_b}{2} + \sqrt{\kappa_b}\nu_{\mathrm{in}}, \tag{D1}$$

$$\dot{\beta} = -i\delta_w\beta - i\mathcal{G}^*\nu - \frac{\kappa_w}{2} + \sqrt{\kappa_w}\beta_{\mathrm{in}}, \tag{D2}$$

where δ_b and δ_w are the buffer and waste frequencies in the frame rotating at the probing frequency, and ν_{in} and β_{in} are the respective input field amplitudes. Now using the relation between the intraresonator fields and the input and output flux $\sqrt{\kappa_b}\nu = \nu_{\mathrm{in}} + \nu_{\mathrm{out}}$, from the equilibrium solution of the coupled system we can extract the transmission coefficient $|S_{21}|^2 = |\beta_{\mathrm{out}}/\nu_{\mathrm{in}}|^2$. Assuming zero input flux on the waste, this leads to

$$|S_{21}|^2 = \left|\frac{2\xi_p\sqrt{\kappa_b\kappa_w\chi_b\chi_w}}{-4\delta_b\delta_w + 2i\delta_b\kappa_w + 2i\delta_w\kappa_b + \kappa_b\kappa_w + \chi_b\chi_w\xi_p^2}\right|^2, \tag{D3}$$

or with the respect to the cooperativity $C = 4(\chi_b\chi_w/\kappa_w\kappa_b)$,

$$|S_{21}|^2 = \frac{4C}{\left|-\frac{4\delta_b\delta_w}{\kappa_b\kappa_w} + 2i\frac{\delta_b}{\kappa_b} + 2i\frac{\delta_w}{\kappa_w} + 1 + C\right|^2}. \tag{D4}$$

This expression can be directly related to the detector efficiency $\eta_{4\mathrm{wm}}$ as the input photon frequency is varied. The FWHM of $|S_{21}|^2$,

$$\kappa_d = \sqrt{2}\sqrt{\sqrt{\kappa_b^2\kappa_w^2 + \left(\frac{\kappa_b - \kappa_w}{2}\right)^4} - \left(\frac{\kappa_b - \kappa_w}{2}\right)^2}, \tag{D5}$$

gives the bandwidth of the detector.

APPENDIX E: TRANSMISSION COEFFICIENT IN PRESENCE OF BUFFER RESONATOR LOSSES

The effect of the buffer resonator internal losses on the efficiency $\eta_{4\mathrm{wm}}$ can be evaluated by inserting $\kappa_{\mathrm{tot}} = \kappa_{b,\mathrm{int}} + \kappa_{b,\mathrm{ext}}$ (internal and coupling losses) into Eq. (D1). Assuming that the incoming photon and the pump frequencies are optimally tuned (i.e., $\delta_b = \delta_w = 0$), the transmission coefficient becomes

$$|S_{21}|^2 = \frac{4\mathcal{C}}{\left(\frac{\kappa_{b,\mathrm{int}}}{\kappa_{b,\mathrm{ext}}} + 1 + \mathcal{C}\right)^2}. \tag{E1}$$

The maximization of $|S_{21}|^2$ with respect to the cooperativity C yields

$$|S_{21}|^2 \leq \frac{1}{1 + \frac{\kappa_{b,\mathrm{int}}}{\kappa_{b,\mathrm{ext}}}}. \tag{E2}$$

The internal losses of the buffer resonator $\kappa_{b,\mathrm{int}}/2\pi = 0.028$ MHz, combined with the external (coupling) losses $\kappa_{b,\mathrm{ext}}/2\pi = 0.172$ MHz, give the maximum efficiency of the main text, $\eta_{4\mathrm{wm}} = 0.86$.

APPENDIX F: JOHNSON-NYQUIST NOISE

The thermal noise detected in the main text is described by a Johnson-Nyquist noise. In the classical framework,

the noise power is expressed as a function of the detector bandwidth Δf and the temperature T of the experiment: $P_{\text{th}} = k_b T \Delta f$. In the quantum regime relevant to our experiment performed at low temperature 10 mK ($k_b T \ll \hbar\omega_b$), the average energy provided by the modes is given by Bose-Einstein statistics such as $k_b T \to \hbar\omega\bar{n}_b$, where $\bar{n}_b = 1/(e^{\hbar\omega_/k_b T} - 1)$ is the number of photons per mode. The expression describing the flux of thermal photons per second is then

$$\frac{P_{\text{th}}}{\hbar\omega_b} = \bar{n}_b \Delta f \,. \tag{F1}$$

To extract the extra number of clicks α_{th} induced by this photon flux, we must take into account its conversion efficiency, which depends on the total detector efficiency η, but also on its frequency detuning with the buffer resonator. In the limit where $\kappa_b \ll \kappa_w$, we can consider that the conversion efficiency $|S_{21}|^2(f)$ is given by a Lorentzian function centered around $f_b = \omega_b/2\pi$ with an FWHM $\kappa_d/2\pi$. This assumption yields the total number of extra clicks during a detection window:

$$\begin{aligned}\alpha_{\text{th}} &= \int_{-\infty}^{+\infty} \frac{\bar{n}_b \eta}{1 + \left(\frac{f - f_b}{\kappa_d/(4\pi)}\right)^2} df \\ &= \frac{\bar{n}_b \eta \kappa_d}{4}.\end{aligned} \tag{F2}$$

APPENDIX G: OPTIMIZATION OF THE DETECTION TIME T_d

In the main text, we define the qubit efficiency as $\eta_{\text{qubit}} = (T_1/T_d)(1 - e^{-T_d/T_1})$. This expression can approach close to 1 by shortening the detection window, thereby diminishing the ratio T_d/T_1. Nevertheless, reducing T_d also decreases the duty cycle η_D. One thus has to find a tradeoff between η_D and η_{qubit} by maximizing the product

$$\eta_D \eta_{\text{qubit}} = \frac{T_1}{T_m + T_r + T_d}(1 - e^{-T_d/T_1}). \tag{G1}$$

In the limit where $T_m + T_r \ll T_d \ll T_1$, the product $\eta_D \eta_{\text{qubit}}$ takes the simple form

$$\eta_D \eta_{\text{qubit}} \approx \left(1 - \frac{T_m + T_r}{T_d}\right)\left(1 - \frac{T_d}{2T_1}\right). \tag{G2}$$

The optimal detection window is then equal to

$$T_d \approx \sqrt{2(T_m + T_r)T_1}. \tag{G3}$$

Taking into account the parameters of our system, we choose $T_d = 10\ \mu\text{s}$.

APPENDIX H: EFFECT OF QUBIT RELAXATION TIME IMPROVEMENT ON SMPD SENSITIVITY

In the main text, we assert that augmenting the qubit's T_1 is a pivotal factor in advancing the detector's sensitivity to a great extent. Indeed, an extended T_1 inherently enhances the efficiency of the qubit, η_{qubit}. Furthermore, under the assumption of a constant $T_r + T_m$, from Eq. (G3), it becomes apparent that the optimal detection time rises, thereby amplifying the duty cycle η_D. An extended relaxation time contributes also to heightened readout efficiency, η_{RO}. It becomes possible to increase the readout time, T_r, without encountering adverse effects from relaxation events during measurement. This naturally enhances the distinction between the two states within the phase plane.

The qubit relaxation time also plays a role in the SMPD dark count rate, as it appears directly in $\alpha_{\text{qubit}} = (p_{\text{eq}}/T_1)\eta_D + (p_{\text{reset}}/T_{\text{cycle}})$ and indirectly in $\alpha_{\text{th}} = (\kappa_d/4)\eta\bar{n}_b$ involving the total efficiency η.

Assuming that the T_1 of the device presented in the main text is larger by an order of magnitude, it follows that $\eta_{\text{qubit}}, \eta_{\text{RO}}, \eta_D \sim 1$ and $\eta \sim \eta_{4\text{wm}}$. Concerning the dark count rate, $\alpha_{\text{qubit}} \sim 0\ \text{s}^{-1}$ and $\alpha \sim \alpha_{\text{th}}$.

Under these conditions, we can estimate that the new sensitivity would be $\mathcal{S}_{\text{high}T_1} = 6.8 \times 10^{-23}\ \text{W}/\sqrt{\text{Hz}}$ (compared with the actual sensitivity $\mathcal{S} = 10^{-22}\ \text{W}/\sqrt{\text{Hz}}$).

To further improve the sensitivity of the detector, it is crucial to reduce the dark count rate due to the thermal population of the line. As mentioned in the main text, one option is to reduce the bandwidth of the detector to match the bandwidth of the system being measured. A detailed study of the dark count rate behavior with the respect to the bandwidth of the SMPD is given in Ref. [43].

APPENDIX I: TWIN SMPD DEVICE

In the main text we present the characterization of our first working device (SMPD1) with a sensitivity $\mathcal{S} = 10^{-22}\ \text{W}/\sqrt{\text{Hz}}$. A twin device (SMPD2) was fabricated a few months later to be used in a spin detection experiment [8]. Its resonator frequencies ($\omega_b/2\pi = 7.459$ GHz unbiased, $\omega_w/2\pi = 8.004$ GHz) and qubit frequency ($\omega_q/2\pi = 6.193$ GHz) were chosen to optimize the detector performances around 7.3 GHz. The qubit has a

TABLE II. Details of efficiency and dark count rate for SMPD1 and SMPD2.

Device	α_{qubit} (s^{-1})	$\alpha_{4\text{wm}}$ (s^{-1})	α_{th} (s^{-1})	
SMPD1	5	/	80	
SMPD2	9	2	90	
	η_D	η_{RO}	$\eta_{4\text{wm}}$	η_{qubit}
SMPD1	0.84	0.76	0.86	0.84
SMPD2	0.79	0.90	0.69	0.73

smaller lifetime, $T_1 = 15$ µs, and a comparable equilibrium population, $p_{eq} = 2 \times 10^{-4}$. The measured efficiency, $\eta = 0.32$, and the measured dark count rate, $\alpha = 103$ s^{-1}, give an absolute sensitivity $\mathcal{S} = 1.5 \times 10^{-22}$ W/$\sqrt{\text{Hz}}$ at 7.3 GHz. Table II shows the efficiency and dark count budget of SMPD2 and how it compares with SMPD1.

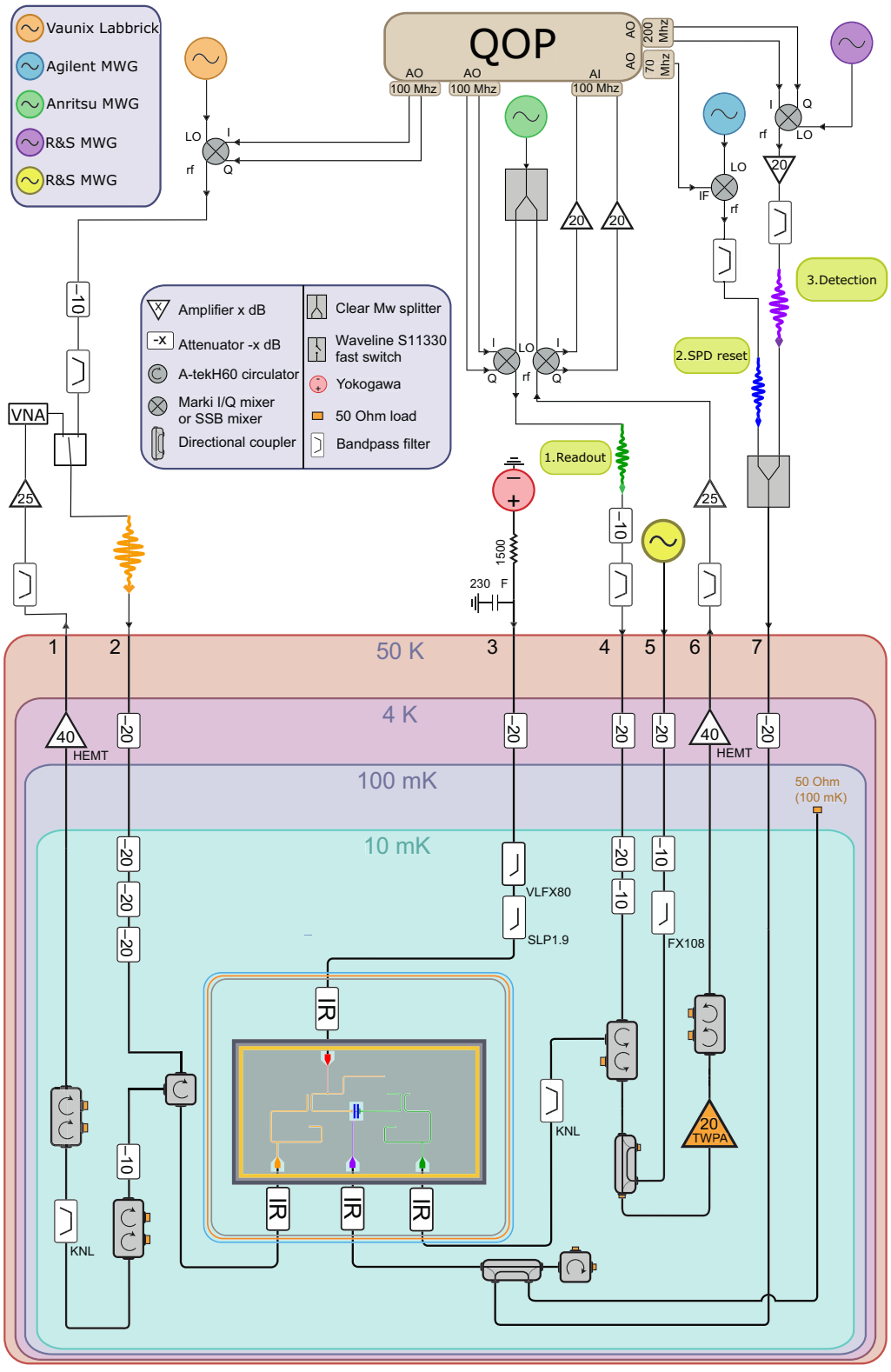

FIG. 6. Schematic of the setup. Wiring and all the components used in this experiment at room temperature and cryogenic temperature are shown.

The decrease in η_D and η_{qubit} is due to the shorter T_1, while the increase in η_{RO} is due to a cleaner calibration of the parametric amplifier. The SMPD2 buffer resonator presents higher internal losses which translate into a smaller $\eta_{4\text{wm}}$.

APPENDIX J: CRYOGENIC SETUP

Figure 6 shows the wiring of the cryogenic setup used in this experiment. Lines 1 and 2 correspond to the detector input. They are used both to characterize the parameters of the buffer resonator (ω_b, κ_b) and to calibrate the detector efficiency by sending a well-controlled number of photons. Line 3 is a dc flux bias line for tuning the SQUID inductance, which controls the frequency ω_b of the buffer resonator. Lines 4, 5, and 6 are used to probe the waste resonator to perform a dispersive readout of the qubit. Line 7 corresponds to the qubit drive.

[1] M. Orrit and J. Bernard, Single pentacene molecules detected by fluorescence excitation in a p-terphenyl crystal, Phys. Rev. Lett. **65**, 2716 (1990).

[2] T. A. Klar, S. Jakobs, M. Dyba, A. Egner, and S. W. Hell, Fluorescence microscopy with diffraction resolution barrier broken by stimulated emission, Proc. Nat. Acad. Sci. **97**, 8206 (2000).

[3] E. Betzig, G. H. Patterson, R. Sougrat, O. W. Lindwasser, S. Olenych, J. S. Bonifacino, M. W. Davidson, J. Lippincott-Schwartz, and H. F. Hess, Imaging intracellular fluorescent proteins at nanometer resolution, Science **313**, 1642 (2006).

[4] C. Bruschini, H. Homulle, I. M. Antolovic, S. Burri, E. Charbon, Single-photon avalanche diode imagers in biophotonics: Review and outlook, Light: Sci. Appl. **8**, 87 (2019).

[5] R. H. Hadfield, Single-photon detectors for optical quantum information applications, Nat. Photonics **3**, 696 (2009).

[6] E. Albertinale, L. Balembois, E. Billaud, V. Ranjan, D. Flanigan, T. Schenkel, D. Estève, D. Vion, P. Bertet, and E. Flurin, Detecting spins by their fluorescence with a microwave photon counter, Nature **600**, 434 (2021).

[7] E. Billaud, L. Balembois, M. L. Dantec, M. Rančić, E. Albertinale, S. Bertaina, T. Chanelière, P. Goldner, D. Estève, D. Vion, P. Bertet, and E. Flurin, Microwave fluorescence detection of spin echoes, arxiv:2208.13586 [quant-ph].

[8] Z. Wang, L. Balembois, M. Rančić, E. Billaud, M. L. Dantec, A. Ferrier, P. Goldner, S. Bertaina, T. Chanelière, D. Estève, D. Vion, P. Bertet, and E. Flurin, Single-electron spin resonance detection by microwave photon counting, Nature **619**, 276 (2023).

[9] S. K. Lamoreaux, K. A. van Bibber, K. W. Lehnert, and G. Carosi, Analysis of single-photon and linear amplifier detectors for microwave cavity dark matter axion searches, Phys. Rev. D **88**, 035020 (2013).

[10] A. V. Dixit, S. Chakram, K. He, A. Agrawal, R. K. Naik, D. I. Schuster, and A. Chou, Searching for dark matter with a superconducting qubit, Phys. Rev. Lett. **126**, 141302 (2021).

[11] M. Scigliuzzo, A. Bengtsson, J.-C. Besse, A. Wallraff, P. Delsing, and S. Gasparinetti, Primary thermometry of propagating microwaves in the quantum regime, Phys. Rev. X **10**, 041054 (2020).

[12] R. Assouly, R. Dassonneville, T. Peronnin, A. Bienfait, and B. Huard, Quantum advantage in microwave quantum radar, Nat. Phys. **19**, 1418 (2023).

[13] R. Raussendorf, D. E. Browne, and H. J. Briegel, Measurement-based quantum computation on cluster states, Phys. Rev. A **68**, 022312 (2003).

[14] H. J. Briegel, D. E. Browne, W. Dür, R. Raussendorf, and M. Van den Nest, Measurement-based quantum computation, Nat. Phys. **5**, 19 (2009).

[15] S. Bartolucci, P. Birchall, H. Bombin, H. Cable, C. Dawson, M. Gimeno-Segovia, E. Johnston, K. Kieling, N. Nickerson, M. Pant, F. Pastawski, T. Rudolph, and C. Sparrow, Fusion-based quantum computation, arxiv:2101.09310 [quant-ph].

[16] A. Narla, S. Shankar, M. Hatridge, Z. Leghtas, K. Sliwa, E. Zalys-Geller, S. Mundhada, W. Pfaff, L. Frunzio, R. Schoelkopf, and M. Devoret, Robust concurrent remote entanglement between two superconducting qubits, Phys. Rev. X **6**, 031036 (2016).

[17] A. Opremcak, I. V. Pechenezhskiy, C. Howington, B. G. Christensen, M. A. Beck, E. Leonard, J. Suttle, C. Wilen, K. N. Nesterov, G. J. Ribeill, T. Thorbeck, F. Schlenker, M. G. Vavilov, B. L. T. Plourde, and R. McDermott, Measurement of a superconducting qubit with a microwave photon counter, Science **361**, 1239 (2018).

[18] J.-C. Besse, S. Gasparinetti, M. C. Collodo, T. Walter, A. Remm, J. Krause, C. Eichler, and A. Wallraff, Parity detection of propagating microwave fields, Phys. Rev. X **10**, 011046 (2020).

[19] G. Romero, J. J. García-Ripoll, and E. Solano, Microwave photon detector in circuit QED, Phys. Rev. Lett. **102**, 173602 (2009).

[20] F. Helmer, M. Mariantoni, E. Solano, and F. Marquardt, Quantum nondemolition photon detection in circuit QED and the quantum Zeno effect, Phys. Rev. A **79**, 052115 (2009).

[21] S. R. Sathyamoorthy, L. Tornberg, A. F. Kockum, B. Q. Baragiola, J. Combes, C. Wilson, T. M. Stace, and G. Johansson, Quantum nondemolition detection of a propagating microwave photon, Phys. Rev. Lett. **112**, 093601 (2014).

[22] O. Kyriienko and A. S. Sørensen, Continuous-wave single-photon transistor based on a superconducting circuit, Phys. Rev. Lett. **117**, 140503 (2016).

[23] S. R. Sathyamoorthy, T. M. Stace, and G. Johansson, Detecting itinerant single microwave photons, Comptes Rendus Phys. **17**, 756 (2016).

[24] X. Gu, A. F. Kockum, A. Miranowicz, Y.-x. Liu, and F. Nori, Physics Reports Microwave photonics with superconducting quantum circuits, Phys. Rep. **718–719**, 1 (2017).

[25] C. H. Wong and M. G. Vavilov, Quantum efficiency of a single microwave photon detector based on a semiconductor double quantum dot, Phys. Rev. A **95**, 012325 (2017).

[26] B. Royer, A. L. Grimsmo, A. Choquette-Poitevin, and A. Blais, Itinerant microwave photon detector, Phys. Rev. Lett. **120**, 203602 (2018).
[27] A. L. Grimsmo, B. Royer, J. M. Kreikebaum, Y. Ye, K. O'Brien, I. Siddiqi, and A. Blais, arXiv:2005.06483 [quant-ph].
[28] Y.-F. Chen, D. Hover, S. Sendelbach, L. Maurer, S. T. Merkel, E. J. Pritchett, F. K. Wilhelm, and R. McDermott, Microwave photon counter based on Josephson junctions, Phys. Rev. Lett. **107**, 217401 (2011).
[29] K. Koshino, K. Inomata, T. Yamamoto, and Y. Nakamura, Implementation of an impedance-matched Γ system by dressed-state engineering, Phys. Rev. Lett. **111**, 153601 (2013).
[30] K. Inomata, Z. Lin, K. Koshino, W. D. Oliver, J.-S. Tsai, T. Yamamoto, and Y. Nakamura, Single microwave-photon detector using an artificial Γ-type three-level system, Nat. Commun. **7**, 12303 (2016).
[31] J.-C. Besse, S. Gasparinetti, M. C. Collodo, T. Walter, P. Kurpiers, M. Pechal, C. Eichler, and A. Wallraff, Single-shot quantum nondemolition detection of individual itinerant microwave photons, Phys. Rev. X **8**, 021003 (2018).
[32] S. Kono, K. Koshino, Y. Tabuchi, A. Noguchi, and Y. Nakamura, Quantum non-demolition detection of an itinerant microwave photon, Nat. Phys. **14**, 546 (2018).
[33] G.-H. Lee, D. K. Efetov, W. Jung, L. Ranzani, E. D. Walsh, T. A. Ohki, T. Taniguchi, K. Watanabe, P. Kim, D. Englund, and K. C. Fong, Graphene-based Josephson junction microwave bolometer, Nature **586**, 42 (2020).
[34] D. I. Schuster, A. A. Houck, J. A. Schreier, A. Wallraff, J. M. Gambetta, A. Blais, L. Frunzio, J. Majer, B. Johnson, M. H. Devoret, S. M. Girvin, and R. J. Schoelkopf, Resolving photon number states in a superconducting circuit, Nature **445**, 515 (2007).
[35] S. Gleyzes, S. Kuhr, C. Guerlin, J. Bernu, S. Deléglise, U. Busk Hoff, M. Brune, J.-M. Raimond, and S. Haroche, Quantum jumps of light recording the birth and death of a photon in a cavity, Nature **446**, 297 (2007).
[36] R. Lescanne, S. Deléglise, E. Albertinale, U. Réglade, T. Capelle, E. Ivanov, T. Jacqmin, Z. Leghtas, and E. Flurin, Irreversible qubit-photon coupling for the detection of itinerant microwave photons, Phys. Rev. X **10**, 021038 (2020).
[37] E. A. Sete, J. M. Martinis, and A. N. Korotkov, Quantum theory of a bandpass Purcell filter for qubit readout, Phys. Rev. A **92**, 012325 (2015).
[38] K. Serniak, M. Hays, G. de Lange, S. Diamond, S. Shankar, L. D. Burkhart, L. Frunzio, M. Houzet, and M. H. Devoret, Hot nonequilibrium quasiparticles in transmon qubits, Phys. Rev. Lett. **121**, 157701 (2018).
[39] K. Serniak, S. Diamond, M. Hays, V. Fatemi, S. Shankar, L. Frunzio, R. Schoelkopf, and M. Devoret, Direct dispersive monitoring of charge parity in offset-charge-sensitive transmons, Phys. Rev. Appl. **12**, 014052 (2019).
[40] X. Y. Jin, A. Kamal, A. P. Sears, T. Gudmundsen, D. Hover, J. Miloshi, R. Slattery, F. Yan, J. Yoder, T. P. Orlando, S. Gustavsson, and W. D. Oliver, Thermal and residual excited-state population in a 3D transmon qubit, Phys. Rev. Lett. **114**, 240501 (2015).
[41] T. Connolly, P. D. Kurilovich, S. Diamond, H. Nho, C. G. L. Bøttcher, L. I. Glazman, V. Fatemi, and M. H. Devoret, arXiv:2302.12330 [quant-ph] (2023).
[42] J. Gambetta, A. Blais, D. I. Schuster, A. Wallraff, L. Frunzio, J. Majer, M. H. Devoret, S. M. Girvin, and R. J. Schoelkopf, Qubit-photon interactions in a cavity: Measurement-induced dephasing and number splitting, Phys. Rev. A **74**, 042318 (2006).
[43] L. Balembois, thesis, Paris Saclay, 2023.
[44] A. P. M. Place *et al.*, New material platform for superconducting transmon qubits with coherence times exceeding 0.3 milliseconds, Nat. Commun. **12**, 1779 (2021).
[45] C. Wang *et al.*, Towards practcial quantum computers: transmon qubit with a lifetime approaching 0.5 milliseconds, npj Quantum Inf. **8**, 3 (2022).